

Merged-beams Reaction Studies of $\text{O} + \text{H}_3^+$

N. de Ruelle^{1,2}, K. A. Miller¹, A. P. O'Connor^{1,3}, X. Urbain⁴, C. F. Buzard⁵, S.
Vissapragada¹, and D. W. Savin¹

Received _____; accepted _____

arXiv:1508.07882v1 [astro-ph.IM] 31 Aug 2015

¹Columbia Astrophysics Laboratory, Columbia University, New York, NY 10027, U.S.A.

²Present address: Department of Physics, Stockholm University, Stockholm,
106 91, Sweden

³Present address: Max-Planck Institute for Nuclear Physics, Heidelberg 69117, Germany

⁴Institute of Condensed Matter and Nanosciences, Université catholique de Louvain,
B-1348 Louvain-la-Neuve, Belgium

⁵Barnard College, Columbia University, New York, NY 10027, U.S.A.

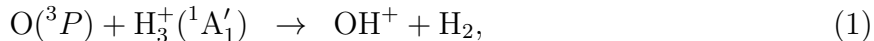
ABSTRACT

We have measured the reaction of $\text{O} + \text{H}_3^+$ forming OH^+ and H_2O^+ . This is one of the key gas-phase astrochemical processes initiating the formation of water molecules in dense molecular clouds. For this work, we have used a novel merged fast-beams apparatus which overlaps a beam of H_3^+ onto a beam of ground-term neutral O. Here, we present cross section data for forming OH^+ and H_2O^+ at relative energies from ≈ 3.5 meV to ≈ 15.5 and 0.13 eV, respectively. Measurements were performed for statistically populated $\text{O}(^3P_J)$ in the ground term reacting with hot H_3^+ (with an internal temperature of $\sim 2500 - 3000$ K). From these data, we have derived rate coefficients for translational temperatures from ≈ 25 K to $\sim 10^5$ and 10^3 K, respectively. Using state-of-the-art theoretical methods as a guide, we have converted these results to a thermal rate coefficient for forming either OH^+ or H_2O^+ , thereby accounting for the temperature dependence of the O fine-structure levels. Our results are in good agreement with two independent flowing afterglow measurements at a temperature of ≈ 300 K, and with a corresponding level of H_3^+ internal excitation. This good agreement strongly suggests that the internal excitation of the H_3^+ does not play a significant role in this reaction. The Langevin rate coefficient is in reasonable agreement with the experimental results at 10 K but a factor of ~ 2 larger at 300 K. The two published classical trajectory studies using quantum mechanical potential energy surfaces lie a factor of ~ 1.5 above our experimental results over this 10 – 300 K range.

Subject headings: astrobiology - astrochemistry - ISM: molecules - methods:
laboratory - molecular data - molecular process

1. Introduction

The genesis of life is believed to depend, in part, on the presence of water. Hence, understanding interstellar formation of H_2O is an important subject for astrochemistry and astrobiology (Klippenstein et al. 2010). Gas-phase formation of water in both diffuse and dense molecular clouds is predicted to involve reactions of neutral O with H_3^+ (Smith & Spanel 1995) via



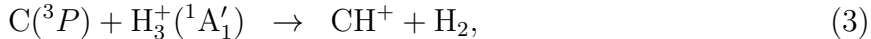
Through a series of subsequent hydrogen abstraction reactions with the abundant H_2 , the ionic products of Reactions (1) and (2) go on to form H_3O^+ . Dissociative recombination of H_3O^+ with electrons results in several possible neutral products, one of which is H_2O . The exact branching ratio for this specific outgoing channel was uncertain for a long time, but has recently been measured to be $\sim 20\%$ (Novotný et al. 2010). At this point, one of the largest remaining uncertainties in the kinetics of the gas-phase formation of water appears to be the lack of reliable rate coefficients for Reactions (1) and (2).

These two reactions also play a role in our understanding of diffuse and dense molecular clouds. The chemistry of these clouds is driven in part by the cosmic ray ionization rate of H_2 (CRIR) ζ . The temperatures of these environments are too cold for neutral-neutral reactions to overcome typical activation barriers. Instead, gas-phase chemistry proceeds largely by ion-neutral reactions (Herbst & Klemperer 1973; Smith & Spanel 1995), a process that is initiated by cosmic ray ionization. The CRIR in diffuse clouds can be inferred using the OH^+ and H_2O^+ abundances. These are affected by Reactions (1) and (2) as described by Hollenbach et al. (2012). In dense clouds ζ is constrained using the measured H_3^+ abundance, which is also affected by Reactions (1) and (2) as is discussed in Klippenstein et al. (2010). Hence, constraining the astrophysical conditions in molecular clouds requires

reliable data for these two reactions.

Published theoretical calculations for these reactions have been carried out using the classical Langevin method (e.g., Milligan & McEwan 2000). Classical trajectory studies using quantum mechanical potential energy surfaces (PESs) have also been published by Bettens et al. (1999) and Klippenstein et al. (2010). These latter two semi-classical results show reasonable agreement between one another. No fully quantum mechanical calculations exist as such calculations for reactions involving four or more atoms are too complex for current capabilities (Althorpe & Clary 2003; Bowman et al. 2011).

Our previous experimental work for the analogous reactions (O’Connor et al. 2015)



suggests that both the classical and semi-classical methods are likely to overestimate the rate coefficient for Reaction (1), underestimate it for Reaction (2), and incorrectly predict the temperature dependence of each. Unfortunately, the published room-temperature, flowing afterglow results for Reactions (1) and (2) cannot resolve this issue due to their large error bars (Milligan & McEwan 2000) and single temperature. Our work here aims to improve our understanding of the $\text{O} + \text{H}_3^+$ reaction and address some of these outstanding issues.

The rest of this paper is organized as follows. In Section 2, we describe briefly our experimental apparatus and method. We present and discuss our results in Section 3 and Section 4, respectively. The astrochemical implications are discussed in Section 5. A summary is given in Section 6.

2. Experimental Apparatus and Method

A detailed description of the ion-neutral merged-beams apparatus used for the present results can be found in O’Connor et al. (2015). Here we provide a brief description of the experiment and method, highlighting mainly those aspects which are new or specific to the present study.

2.1. General

Using a Cs-ion sputter source followed by a Wien filter, we formed a $^{16}\text{O}^-$ beam at a kinetic energy of $E_{\text{O}} \approx 28$ keV (≈ 1.75 keV/amu). This generated a pure beam of $\text{O}^-(^2P)$ as the oxygen anion possesses only a single bound term (Rienstra-Kiracofe et al. 2002). The target material used in the source was Al_2O_3 .

The neutral O beam was produced via photodetachment of the anion inside a floating cell. The kinetic energy of the resulting O beam was controlled by varying the floating cell voltage U_{f} . The cross section for photodetachment of O^- has been measured by Lee & Smith (1979). The electron affinity of oxygen is 1.461 eV (Rienstra-Kiracofe et al. 2002). Using our 808-nm (1.53-eV) laser with ≈ 1.8 kW of power, we estimated that approximately 2% of the anions were converted to ground term $\text{O}(^3P)$. The photon energy and number density were both too low to detach into higher terms.

Similar to the work of Scheer et al. (1998) on photodetachment of C^- , we expect to statistically populate all three levels in the ground term of the atomic oxygen. The $J = 1$ and 0 fine-structure levels lie above the $J = 2$ ground level by 19.6 meV and 28.1 meV, respectively. The thermal population of the J levels can be calculated using the partition functions

$$u_J = \frac{g_J e^{(-E_J/k_{\text{B}}T)}}{\sum_{J'} g_{J'} e^{(-E_{J'}/k_{\text{B}}T)}}. \quad (5)$$

Here $g_J = 2J + 1$ is the statistical weight of level J , k_B is the Boltzmann constant, and T is the temperature. These populations are presented in Figure 1 where one can see that they become statistical at temperatures above ~ 1000 K. In Section 4.2 we explain how we use our results with statistically populated ground-level O to generate thermal rate coefficients.

The molecular beamline begins with a duoplasmatron source from which we extracted a beam of cations and used a Wien filter to charge-to-mass select for H_3^+ . The beam energy of $E_{\text{H}_3^+} \approx 5.29$ keV (≈ 1.75 keV/amu) was chosen to match the velocity of the oxygen anion beam.

The formation mechanism of H_3^+ in a duoplasmatron leads to substantial internal excitation. In our earlier work of C on H_3^+ (O’Connor et al. 2015), we inferred an internal temperature of ~ 2500 K. However, we found good agreement between our thermal rate coefficient results at 1000 K with the mass-scaled results of Savić et al. (2005), who studied C on D_3^+ . Since the work of Savić et al. (2005) used D_3^+ with an internal temperature of 77 K, the good agreement between their results and those of O’Connor et al. (2015) implies that the internal excitation of the H_3^+ does not significantly influence reactions of the type $\text{X} + \text{H}_3^+ \rightarrow \text{XH}_n^+ + \text{H}_{3-n}$ for $n = 1$ or 2. We expect that this will also be the case for O on H_3^+ and will return to this issue in Section 4.3.

In order to improve the H_3^+ beam quality in the interaction region, we have modified the beamline just before the cylindrical deflector used to merge the cation beam onto the neutral beam. In specific, we installed a set of XY steerers and adjusted the location of the one-dimensional (1D) electrostatic lens before the merger. To compensate for the lack of vertical focusing in the cylindrical deflector, we used one pair of vertical steerer plates for focusing. One of the horizontal steering plates was used to adjust the angle of the beam going into the 1D lens and cylindrical deflector. All of the other steerer plates were grounded. Additionally, the 1D lens was moved closer to the cylindrical deflector so that we

could focus the beam at the appropriate location inside the deflector in order to generate a parallel beam at the exit (i.e., at the beginning of the interaction region). The resulting H_3^+ current in the interaction region was typically ~ 225 nA, corresponding to a typical number density of $\sim 10^5$ cm^{-3} .

In the interaction region, the kinetic energy of any product ions formed was essentially the sum of E_{O} plus the product of the H_3^+ kinetic energy per amu (≈ 1.75 keV/amu) times the mass in amu transferred from the H_3^+ . For O at 28 keV, the kinetic energy of the product was 29.75 keV for forming OH^+ , Reaction (1), and 31.5 keV for H_2O^+ , Reaction (2). At the end of the interaction region, the beams continued into a chicane which directed the H_3^+ into a Faraday cup where the current was recorded. The daughter products were directed through the chicane and continue into an electrostatic energy analyzer. This consisted of a series of three 90° cylindrical deflectors with voltages optimized to direct the desired product ions into a channel electron multiplier (CEM). This final analyzer also served to discriminate against the dominant charged particle background which was due to the ~ 28 keV O^+ formed by stripping of the O beam on the residual gas downstream of the cation beam merger. The transmittance from the interaction region to the CEM was measured to be $T_{\text{a}} = 0.74 \pm 0.02$. Here and throughout all uncertainties are quoted at an estimated 1σ statistical confidence level.

2.2. Neutral Detector

The neutral beam current I_{O} is monitored by measuring the secondary negative particle emission from a target inside a neutral particle detector (Bruhns et al. 2010a) and is given by

$$I_{\text{O}} = \frac{I_{\text{ND}}}{\gamma T_{\text{n}}}. \quad (6)$$

Here I_{ND} is the current measured on the neutral detector, γ is the secondary negative particle emission coefficient, and T_n is the transmission into the detector. Typical values for I_{O} are ~ 23 nA, as measured in amperes, with a statistical-like uncertainty of 5%. These currents correspond to particle number densities of $\sim 10^4$ cm $^{-3}$.

We determined γ using collisional detachment of O^- on helium introduced into the chicane by a leak valve. This converts a portion of the initial O^- beam to O and O^+ . The positive and negative currents, I_{O^-} and I_{O^+} , respectively, were measured in a Faraday cup, called the upper cup, which is situated behind a hole in the outer plate of the middle cylindrical deflector of the final analyzer. Because of the design of the final analyzer we can measure either I_{O^-} or I_{O^+} in the upper cup simultaneous with I_{ND} , but not all three together. The transmittance from the interaction region into the upper cup was measured to be $T_{\text{u}} = 0.64 \pm 0.04$.

The total particle flux is assumed to be conserved at any given helium pressure p . This gives

$$I_{\text{O}^-}(p=0) + I_{\text{O}}(p=0) + I_{\text{O}^+}(p=0) = I_{\text{O}^-}(p) + I_{\text{O}}(p) + I_{\text{O}^+}(p), \quad (7)$$

where collisional detachment on the residual gas in the system generates non-zero currents of O and O^+ at $p=0$. All of the currents are taken as positive quantities. In terms of measured quantities, we can rewrite Equation (7) as

$$\frac{I_{\text{O}^-}^{\text{u}}(0)}{T_{\text{u}}} + \frac{I_{\text{ND}}(0)}{\gamma T_{\text{n}}} + \frac{I_{\text{O}^+}^{\text{u}}(0)}{T_{\text{u}}} = \frac{I_{\text{O}^-}^{\text{u}}(p)}{T_{\text{u}}} + \frac{I_{\text{ND}}(p)}{\gamma T_{\text{n}}} + \frac{I_{\text{O}^+}^{\text{u}}(p)}{T_{\text{u}}}, \quad (8)$$

where I^{u} stands for the currents measured in the upper cup. Rearranging this yields

$$\gamma = \frac{-\Delta I_{\text{ND}}(p)}{\Delta I_{\text{O}^-}^{\text{u}}(p) + \Delta I_{\text{O}^+}^{\text{u}}(p)} \frac{T_{\text{u}}}{T_{\text{n}}} \quad (9)$$

where $\Delta I(p) = I(p) - I(0)$. Typically we measure $\Delta I_{\text{O}^-}^{\text{u}}$ and ΔI_{ND} at set of a pressures p_i . Due to the coarse control on our leak valve, we measure $\Delta I_{\text{O}^+}^{\text{u}}$ and ΔI_{ND} at a slightly different set of pressures p_k . Here we were able to match the pressures p_i and p_k to

better than 3%. This small difference introduces an insignificant uncertainty into our γ determination. So we can convert these p_k results to those for p_i using

$$\Delta I_{\text{O}^+}^{\text{u}}(p_i) = \Delta I_{\text{O}^+}^{\text{u}}(p_k) \frac{\Delta I_{\text{ND}}(p_i)}{\Delta I_{\text{ND}}(p_k)} \quad (10)$$

which we can then substitute into Equation (9).

To determine γ , we measured I_{O^-} and I_{ND} simultaneously over intervals of ~ 250 s. First, no gas was introduced in the chicane ($p = 0$). Next, we measured with a helium pressure of p_i . Lastly, we measured again without helium. For the currents measured without gas, we used the average of the before and after measurements. This allows us to take into account the fluctuations of the O^- beam during the measurement. For each current measured at high pressure, we took the average of the current over the 250 s interval. We repeated this pattern to measure I_{ND} and $I_{\text{O}^+}^{\text{u}}$ at p_k . Over the several months of our $\text{O} + \text{H}_3^+$ measurement campaign, we monitored γ periodically and found $\gamma = 2.6 \pm 0.3$. The uncertainty in γ is treated as a systematic error.

2.3. Beam Overlap and Relative Energies

The overlap integral of the two beams has been determined using a combination of beam profile measurements in the interaction region and geometric modeling, as described in Bruhns et al. (2010b) and O’Connor et al. (2015). A typical average bulk misalignment between the two beams of 0.38 mrad was determined from the measured beam profiles. This represents a factor-of-two reduction compared to our $\text{C} + \text{H}_3^+$ work and is a result of the modifications of the cation beamline described in Section 2.1.

The average relative energy $\langle E_r \rangle$, along with the corresponding energy spread, was determined from the beam profiles measurements and a Monte-Carlo simulation of the beams trajectories described in O’Connor et al. (2015). Figure 2 shows the results

values for $\langle E_r \rangle$ and the corresponding uncertainty. Based on these simulations, the lowest average relative energy achieved here is ≈ 3.5 meV, corresponding to an effective translational temperature of ≈ 27 K (as derived from a Maxwell-Boltzmann fit of the velocity distribution). We also find a Gaussian distribution for the interaction angle with a mean value of $\langle \theta \rangle = 0.71 \pm 0.34$ mrad. These improvements over O’Connor et al. (2015) are a direct result of the reduced bulk misalignment between the two beams.

2.4. Merged-beams Rate Coefficient

The measured merged-beams rate coefficient is the product of the cross section σ and the relative velocity v_r convolved with the energy spread of the experiment and is given by

$$\langle \sigma v_r \rangle = \frac{S}{T_a T_g \eta} \frac{e^2 v_n v_i}{I_n I_i} \frac{1}{L \langle \Omega(z) \rangle}. \quad (11)$$

Here S is the signal count rate; T_g is the geometrical transmittance of the grid in front of the CEM; η is the efficiency of the CEM; e is the elementary charge; v_n and v_i are the laboratory velocities of the neutral and molecular ion beams, respectively; I_n and I_i are the neutral and ion beam currents, respectively; L is the interaction region length; and $\langle \Omega(z) \rangle$ is the overlap integral of the two beams in the interaction region. Typical values of all these parameters and their uncertainties are listed in Tables 1 and 2. Details about the associated uncertainties as well as the data acquisition procedure can be found in O’Connor et al. (2015).

3. Experimental Results

Our results for the merged-beams rate coefficient are presented in Figure 3 as a function of $\langle E_r \rangle$ for Reactions (1) and (2). Data were collected for merged-beam rate coefficient values down to $\sim 1 \times 10^{-10}$ cm³ s⁻¹, below which the decreasing signal-to-noise

ratio made the required data acquisition times prohibitively long. From these, and using our calculated experimental energy spread, we can extract the cross section for each reaction for statistically populated ground-term O. We then generate translational temperature rate coefficients for each reaction by convolving the extracted cross section with a Maxwell-Boltzmann distribution describing the reaction center-of-mass velocity distribution. However, the internal energies of the reactants are not in thermal equilibrium. In Section 4.2 we describe how we can convert our translational temperature results into a thermal rate coefficient relevant for astrochemistry where the internal energies of the reactants are typically in thermal equilibrium.

3.1. Cross Sections

The cross section σ_x can be extracted from our data using the fitting function

$$\sigma_x = \frac{a_0 + a_{1/2}E^{1/2}}{E^{2/3} + b_1E + b_2E^2 + b_4E^4}. \quad (12)$$

Here x refers to either Reaction (1) or (2), σ_x is in units of cm^2 , and E is in eV. This function includes a term with an $E^{-2/3}$ behavior at low energies that was chosen to match the predicted $T^{-1/6}$ dependence in the thermal rate coefficient at low temperatures due to the charge-quadrupole interaction (Klippenstein et al. 2010). The other powers of E have been arbitrarily chosen to match the higher energy dependence in the measured merged-beams rate coefficients.

To fit our measured data, we multiplied Equation (12) by v_r and convolved the product with the experimental relative velocity distribution. The best fits to the data are shown in Figure 3 by the solid lines. Table 3 gives the best fit parameters of the cross section for each reaction. The accuracy of the fit for Reaction (1) is better than 7%. For Reaction (2), the accuracy is better than 15%. Figure 4 shows the experimentally derived cross sections

for each reaction. The results have been extrapolated to kinetic energies below ≈ 3.5 meV using the theory of Klippenstein et al. (2010) as a guide.

3.2. Translational Temperature Rate Coefficients

We have derived the translational temperature rate coefficient α_x for each reaction using the product of the extracted cross section σ_x times the relative velocity, all then convolved with a Maxwell-Boltzmann energy distribution. We fit the resulting translational temperature rate coefficient using

$$\alpha_x = \frac{a_0 + a_{1/2}T^{1/2} + a_1T}{T^{1/6} + b_{1/2}T^{1/2} + b_1T + b_{3/2}T^{3/2}} \quad (13)$$

where x refers to either Reaction (1) and (2), α_x is given in units of $\text{cm}^3 \text{s}^{-1}$, and T in units of K. Table 4 gives the best fit parameters for each reaction.

Figure 5 shows the experimentally derived translational temperature rate coefficients and associated uncertainties for Reactions (1) and (2). The uncertainty for each reaction, derived by adding in quadrature the estimated systematic error and the fitting error, is $\approx 14\%$ for Reaction (1) and ranges from $\approx 15 - 27\%$ for Reaction (2), for the respective energy ranges shown in Figure 5. The minimum value achieved for $\langle E_r \rangle$ corresponds to an effective translational temperature of ≈ 27 K, as discussed earlier. The fit function has been chosen so that the extrapolation of the translational temperature rate coefficient below 27 K goes to a $T^{-1/6}$ dependence as predicted by Klippenstein et al. (2010). The highest values of $\langle E_r \rangle$ measured for Reactions (1) and (2) of ≈ 15.5 and 0.13 eV, respectively, yield approximate high temperature limits of $\sim 10^5$ and 10^3 K for the derived translational temperature rate coefficients.

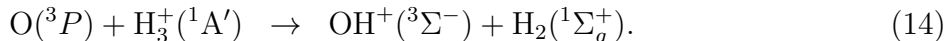
4. Discussion

Figure 6 shows the asymptotic energy limits of various $\text{O} + \text{H}_3^+$ reaction pathways. Reaction (1) is exoergic by ≈ 0.66 eV and Reaction (2), by ≈ 1.70 eV (Milligan & McEwan 2000). The energies are given for all parent and daughter products in their ground symmetries.

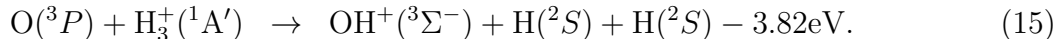
4.1. Merged-beams Rate Coefficients

4.1.1. $\text{O} + \text{H}_3^+ \rightarrow \text{OH}^+ + \text{H}_2$

Taking into account the electronic states and spin symmetries of the reactants and products (Bettens et al. 1999), we can re-write Reaction (1) as



OH^+ can also be formed via the endoergic reaction:

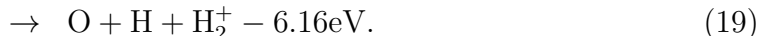
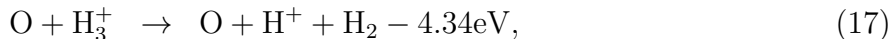


The energy dependence of our measured merged-beams rate coefficient for Reaction (1) has a somewhat similar behavior to that measured for Reaction (3) seen by O’Connor et al. (2015). The merged-beams rate coefficient starts by increasing as the relative energy grows. This behavior could be due to the increasing number of ro-vibrational channels becoming energetically accessible in the reaction products or to the opening up of new electronic states in the intermediate reaction complex. Then, starting at about ≈ 0.9 eV, the energy of the highest value of the merged-beams rate coefficient, there is a suggestion of a complex structure which was not seen in O’Connor et al. (2015). (All of the structures discussed here appears at lower energies than expected, by about 0.9 eV, as we explain in the following

paragraph.) First the competing endoergic channel



appears to open up, resulting in a reduction in the measured merged-beams rate coefficient. This is followed at ~ 3 eV by the opening up of another channel for forming OH^+ , namely Reaction (15), causing a compensating increase in the signal. At higher energies, three additional competing channels open up:



These are followed by a dramatic drop with increasing energy, which we attribute to the competing endoergic reaction pathways taking up all the flux of the reaction.

The shift in these structures to energies lower than the known thresholds most likely comes from the molecular nature of the H_3^+ , with its range of possible ro-vibrational levels contributing to the process (as explained in more detail in O’Connor et al. 2015). This leads to a smearing out of the thresholds with the relative energy, blurring them together for the above-listed endoergic reactions. So we take the highest measured value of the merged-beams rate coefficient, at a relative energy of 0.89 eV, as the opening up of Reaction 16, which would be 1.77 eV for cold H_3^+ . The lower-than-expected energy in the initial decrease of the merged-beams rate coefficient is probably due to the energy available from the internal excitation of H_3^+ in our experiment. The ~ 0.87 eV energy difference lies within the $\sim 0.5 - 1$ eV range inferred from theoretical calculations (Anicich & Futrell 1984) and photodissociation measurements (X. Urbain, private communication). Using the H_3^+ molecular partition function of Kylänpää & Rantala (2011) and specifically their Equation (8), this energy difference gives an internal temperature of ~ 3000 K. This is

slightly higher, but still consistent, with the H_3^+ internal excitation of ~ 2550 inferred in our $\text{C} + \text{H}_3^+$ work which used the same H_3^+ ion source (O’Connor et al. 2015).

4.1.2. $\text{O} + \text{H}_3^+ \rightarrow \text{H}_2\text{O}^+ + \text{H}$

Our merged-beams rate coefficient for Reaction (2) decreases with increasing relative energy. Bettens et al. (1999) describe the formation of H_2O^+ as a two-step process. First a complex is formed where the oxygen atom extracts H^+ from H_3^+ to form an OH^+ ion adjacent to the remaining H_2 . Then the OH^+ and H_2 undergo a relative rotation after which the OH^+ extracts a hydrogen atom from the H_2 . This entire process takes time and could explain the decrease seen in the rate coefficient. As the relative energy increases, the time available for the reaction also decreases. Clearly though, further theoretical and experimental studies are needed to better understand the process.

At ~ 0.1 eV, we observe a strong decrease in the rate coefficient, similar to that of Reaction (4) seen by O’Connor et al. (2015). The endoergic Reactions (15) - (19) are the probable explanation for this drop. The shift to a lower relative energy is also likely due to the internal excitation of H_3^+ .

4.2. Converting Translational Temperature to Thermal Rate Coefficients

In order to convert our translational temperature rate coefficients into a thermal rate coefficient, we follow the approach outlined in O’Connor et al. (2015). This method enables us to correct our results for statistically populated fine-structure levels in the atomic O into data relevant for thermally populated fine-structure levels. In this, we follow the approximations made by Klippenstein et al. (2010), in their calculations for the $\text{O} + \text{H}_3^+$ collision system, namely that the reaction proceeds adiabatically and that surface crossings

and intersystem transitions are both unimportant.

Another assumption that we make is that the internal excitation of the H_3^+ does not affect the reaction. Theoretically, this approach is supported by the long-range character of the entrance PES being dictated by the polarization of the fine-structure state of the oxygen in the field of a point charge (Gentry & Giese 1977). Experimentally, it is supported by the good agreement between our $\text{C} + \text{H}_3^+$ results on internally excited H_3^+ and the mass-scaled results of Savić et al. (2005) for C on D_3^+ with an internal temperature of 77 K. It is also supported by the good agreement that we find below between our thermal $\text{O} + \text{H}_3^+$ results and those of Fehsenfeld (1976) and Milligan & McEwan (2000) for H_3^+ with an internal temperature of 300 K.

Taken all together, these approximations enable us to derive temperature-dependent multiplicative scaling factors to convert our translational temperature results into thermal results. For this we use the theoretical study of Gentry & Giese (1977) for ground term atomic oxygen in the presence of a positive charge. Bettens & Collins (2001) and Klippenstein et al. (2010) also based their calculations on Gentry & Giese (1977), which found that the nine states in the $\text{O}(^3P)$ manifold are split into three attractive and six repulsive surfaces at long-range separation of the reactants. The $M_J = 0$ and ± 1 components of the five-fold degenerate ground state 3P_2 state correlate with the attractive $^3\Sigma$ PES, while the $M_J = \pm 2$ components of the 3P_2 and all components of 3P_1 and 3P_0 , correlate with the repulsive $^3\Pi$ surface. The partition functions for the attractive $^3\Sigma$ and non-reactive $^3\Pi$ PES shown in Figure 7 are given by

$$u_\Sigma = \frac{3}{5}u_2 \tag{20}$$

$$u_\Pi = u_0 + u_1 + \frac{2}{5}u_2 \tag{21}$$

with u_J defined by Equation (5).

The theoretical approach outlined above provides information only for the total

reaction probability, i.e., the sum of Reactions (1) and (2). We are aware of only one published experimental study for the branching ratios for forming OH^+ and H_2O^+ , namely the results of Milligan & McEwan (2000) at 300 K. How those results scale with temperature is uncertain. Indeed, O’Connor et al. (2015) found a significant temperature dependence for the branching ratio in the analogous $\text{C} + \text{H}_3^+$ reaction. Lacking the necessary temperature-dependent information on the branching ratios, in order to convert our translational temperature results to a thermal rate coefficient, we sum our translational temperature rate coefficients for Reactions (1) and (2) and then multiply the result by $3u_\Sigma$. This factor of 3 takes into account the fact that in our measurement only one-third of the O fine-structure levels contribute to the reaction process. The resulting summed thermal rate coefficient is shown in Figure 8.

We can also use this theoretical approach to generate a temperature-dependent Langevin rate coefficient. The classical Langevin rate coefficient of $1.3 \times 10^{-9} \text{ cm}^3 \text{ s}^{-1}$ (Milligan & McEwan 2000), considers all of the $\text{O} + \text{H}_3^+$ symmetries involved in the reaction process to be attractive. We can convert this value to a temperature-dependent thermal rate coefficient by multiplying it by the partition function u_Σ . Both the unmodified and modified Langevin rate coefficient are shown in Figure 8.

4.3. Thermal Rate Coefficients

Our experimentally derived thermal rate coefficient for $\text{O} + \text{H}_3^+$ forming either OH^+ or H_2O^+ is in good agreement with the unmodified Langevin rate coefficient at 10 K. At this temperature, the modified Langevin rate coefficient lies a factor of ≈ 1.6 below our experimental results. This is not surprising since the charge-quadrupole interaction responsible for the growth of the rate coefficient at low temperatures is absent from the Langevin model. As the temperature increases, the unmodified rate coefficient becomes

increasingly discrepant with the experimental results, growing to a factor of ≈ 2 times larger at 300 K. Conversely the modified rate coefficient comes into reasonable agreement with our results, lying just outside the experimental error bars, but matching the general temperature dependence.

The semi-classical results of Bettens et al. (1999) and those of Klippenstein et al. (2010) both shown in Figure 8, each display a trend similar to our experimentally derived thermal rate coefficient. However, both sets of values lie outside our experimental error bars. The Bettens & Collins results are a factor of ≈ 1.7 larger at 10 K and a factor of ≈ 1.3 at 300 K, while the Klippenstein et al. (2010) results are a factor of ≈ 1.4 and 1.7 larger at 10 and 300 K, respectively. The cause for the discrepancy is not clear. For the analogous summed thermal rate coefficient for $\text{C} + \text{H}_3^+$, reasonable agreement was found between our results and the calculations of Bettens & Collins (1998, 2001).

Our derived thermal rate coefficient is in good agreement with the experimental results from Fehsenfeld (1976) at 300 K. In his flowing afterglow experiment, he was unable to distinguish the products of the reaction and thus gave only an overall thermal rate coefficient for O on H_3^+ . Milligan & McEwan (2000) measured the rate coefficients of Reactions (1) and (2) at 295 K. We compare with their summed results and find that their error bar overlaps with ours. So even though their results are a factor of ~ 1.8 times larger than ours, the agreement seems reasonable enough, given the challenge of monitoring the atomic oxygen density in the flowing afterglow method.

Comparing all of the experimental thermal results for O on H_3^+ at ≈ 300 K, we find good agreement between our work with hot H_3^+ (~ 3000 K) and the two published measurements on cold H_3^+ (≈ 300 K). Similarly good agreement was found at a temperature of ~ 1000 K between our $\text{C} + \text{H}_3^+$ work compared to the mass-scaled results of Savić et al. (2005) for $\text{C} + \text{D}_3^+$, which had an internal temperature of 77 K. Taken together, these experimental

results strongly suggest that for reactions of the type $X + H_3^+$, the internal excitation of the H_3^+ does not play a significant role in determining the total rate coefficient for reacting, summed over all possible outgoing channels. We hypothesize that this behavior is due, in part, to the reaction being driven primarily by the long range portion of the PESs for the reaction systems, where the internal excitation of the molecule is not yet felt. Furthermore, H_3^+ has only a single bound electronic symmetry and so the entire population has the same spin symmetry. Thus any spin conservation in the reaction affects the entire H_3^+ population the same way, as opposed to a molecule with a population divided between two or more different spin multiplicities. Clearly, though, further experimental and theoretical work is needed to more solidly understand the physics of the reaction.

5. Astrochemical Implications

We have used the gas-phase astrochemical code Nahoon (Wakelam et al. 2012) and the 2014 version of the KInetic Database for Astrochemistry (KIDA; Wakelam et al. 2015) in order to investigate some of the astrophysical implications of our findings, particularly for the gas-phase chemistry of dense molecular clouds. Though a complete study is beyond the scope of this paper (for example, we leave for future study the effects of surface or ice chemistry as well as any depletion effects), these preliminary models do give some insight into the impact of our results. Following Wakelam et al. (2015), the specific cloud parameters used were a hydrogen nuclei density of $n_H = 2 \times 10^4 \text{ cm}^{-3}$, a CRIR of $\zeta = 10^{-17} \text{ s}^{-1}$, and a visual extinction of $A_V = 30$. We also adopted the initial abundances given in their paper.

For these simulations we have taken our experimentally derived thermal rate coefficient for $O + H_3^+$ for forming either OH^+ or H_2O^+ and implemented it into Nahoon/KIDA. Since the available fitting functions within Nahoon/KIDA were unable to accurately fit our

thermal rate coefficient, we have fit it using the recommended function of Novotný et al. (2013), namely

$$k(T) = A \left(\frac{300 \text{ K}}{T} \right)^n + T^{-3/2} \sum_{i=1}^4 c_i \exp(-T_i/T). \quad (22)$$

The resulting fit parameters are given in Table 5. The deviations of the fitted k from the data are less than $\sim 0.5\%$ over the reported $1 - 10^4$ K temperature range.

We have implemented our thermal rate coefficient into Nahoon/KIDA, modifying Nahoon to handle the above equation. Since we do not know the branching ratios for the formation of OH^+ and H_2O^+ , we have run simulations first assuming a branching ratio of 100% for forming OH^+ and later assuming 100% for forming H_2O^+ . This is justified as both ions are predicted to be highly transitory, rapidly reacting with the abundant H_2 in the cloud to form H_3O^+ via hydrogen abstraction,



As we expected, we found no significant difference in our model results for either branching ratio assumption.

5.1. Formation of Water

To investigate the impact of our results on the formation of water, we have calculated the H_3O^+ and H_2O abundances for a dense molecular cloud at a temperature of 10 K. Over most of the lifetime of a cloud, H_3O^+ is the dominant gas-phase precursor of water, forming H_2O via dissociative recombination



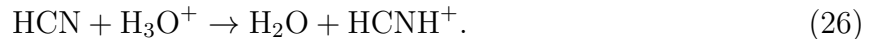
Figure 9 shows the ratios of the predicted abundances using our results relative to those from the unmodified Nahoon/KIDA, which uses the theoretical rate coefficient results of Klippenstein et al. (2010).

At a cloud age of 10^2 years, the abundance of both H_3O^+ and H_2O are reduced by $\approx 15\%$. These changes can be traced back to our reduced rate coefficient for forming OH^+ or H_2O^+ , which go on to H_3O^+ via hydrogen abstraction and then water via dissociative recombination. Naively, one might expect the H_3O^+ and H_2O abundances to be reduced by the ratio of our rate coefficient relative to that of Klippenstein et al. (2010), which is ≈ 0.72 at 10 K. However, our lower rate coefficient results in a reduced destruction rate for the H_3^+ and thus a higher predicted abundance, giving an abundance ratio at 10^2 years of ≈ 1.18 compared to the unmodified Nahoon/KIDA results. Multiplying these two factors together explains the $\approx 15\%$ reduction seen at short times.

At longer times, the observed reductions in H_3O^+ and H_2O become much more significant. Identifying the cause for this, though, is complicated, due to an increase in the complexity of the relevant chemical network. As an example, we discuss here the intermediate times between $\sim 10^{3.5}$ and $10^{5.9}$ years. During this time, along with reaction (24), two additional important channels for forming water open up, namely



and

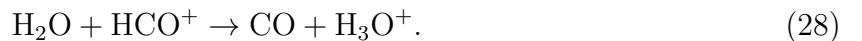


Indeed, these two channels are predicted to dominate over dissociative recombination for part of this epoch. At longer times, dissociative recombination again comes to dominate.

New channels for forming H_3O^+ also open up between $\sim 10^{4.5}$ and $10^{5.8}$ years, including



and



However, these reactions lead to destruction of H_2O as well, since only a fraction of the resulting H_3O^+ gets converted back into water. We find that with the modified chemistry, the larger decrease seen in the relative H_2O abundance (compared to that for H_3O^+) can be traced back, in part, to the increased H_3^+ abundance during this epoch, leading to an enhancement in HCO^+ formation via



The resulting HCO^+ then leads to an increased reduction in the water abundance via reaction (28) for the modified chemistry.

5.2. Cosmic Ray Ionization Rate

In dense molecular clouds, the CRIR ζ can be constrained through observations of the H_3^+ column density (e.g., McCall et al. 1999; Klippenstein et al. 2010; Oka 2013). The H_3^+ is formed in a two-step process, beginning with the ionization of H_2 by cosmic rays; other ionization processes of H_2 are insignificant. At typical dense cloud densities of $n_{\text{H}} \sim 10^4 \text{ cm}^{-3}$, the resulting H_2^+ rapidly reacts with a neutral H_2 molecule, in less than a day (Oka 2013), meaning that H_3^+ generation is completely determined by the CRIR, with a formation rate versus time t of

$$\left[\frac{dn_{\text{H}_3^+}}{dt} \right]_{\text{form}} = \zeta n_{\text{H}_2}, \quad (30)$$

where n_{H_2} is the number density of molecular hydrogen. The dominant destruction mechanisms of H_3^+ in dense clouds are binary chemical reactions with other species, primarily neutral since the electron abundance is too low for dissociative recombination to play a significant role. Thus we can write the destruction rate as

$$\left[\frac{dn_{\text{H}_3^+}}{dt} \right]_{\text{dest}} = \sum_i k_i n_i n_{\text{H}_3^+}, \quad (31)$$

where k_i is the thermal rate coefficient for the reaction of species i with H_3^+ and n_i is the number density of species i .

In the quasi-equilibrium of dense molecular clouds, we can equate Equations (30) and (31) giving

$$\zeta n_{\text{H}_2} = \sum_i k_i n_i n_{\text{H}_3^+}. \quad (32)$$

As described in McCall et al. (1999), Klippenstein et al. (2010), and Oka (2013), the properties of dense clouds enable us to make the approximation

$$N_{\text{H}_3^+} = L n_{\text{H}_3^+}, \quad (33)$$

where $N_{\text{H}_3^+}$ is the observed column density of H_3^+ and L the absorption path length through the cloud. Combining Equations (32) and (33) and rearranging gives

$$\zeta L = \left(\frac{N_{\text{H}_3^+}}{n_{\text{H}_2}} \right) \sum_i k_i n_i. \quad (34)$$

The quantity ζL can thus be constrained by a combination of the observed H_3^+ column density and n_{H_2} number density and astrochemical calculations of the individual terms contributing to the summation over species. Previous studies into Equation (32) have limited the number of species considered. For example, McCall et al. (1999) considered only reactions with CO, Klippenstein et al. (2010) also included O, and Oka (2013) added to these N_2 and electrons. Here we have used the modified Nahoon/KIDA to calculate $\sum_i k_i n_i$ for the most significant species as well as for all species. For comparison, we have also calculated the unmodified Nahoon/KIDA results for all species. Figures 10 and 11, respectively, show our results for cloud ages of 10^5 and 10^6 years over the temperature range of 10 – 400 K. These times lie within the range of commonly inferred cloud ages.

At 10^5 years and below ~ 160 K, the most important reactants with H_3^+ are CO, O, C, H_2O , and the HCN/HNC isomers, in descending order of importance. The contributions

of each of these species are shown by the various colored solid lines in Fig. 10 and the total $\sum_i k_i n_i$ due to all species by the solid black line. Above ~ 250 K, the abundance of C decreases dramatically and reactions with C become unimportant. It is also interesting to note that the structure due to CO largely gets washed out by the contributions of O, C, and H₂O. Additionally, the structures seen in the total $\sum_i k_i n_i$ are due primarily to the HCN/HNC isomers between ~ 120 and 250 K and due to water above 250 K. The increase due to H₂O is a result of the higher temperatures enabling neutral-neutral reactions leading to water to become important. Using the unmodified Nahoon/KIDA yields a total summation shown by the black dashed line, which is up to $\sim 15\%$ larger than the modified value.

At 10^6 years and below ~ 240 K the most important reactants with H₃⁺ are CO, O, and N₂, in decreasing order of importance. The contributions of each of these species are shown by the various colored solid lines in Fig. 11 and the total $\sum_i k_i n_i$ due to all species by the solid black line. Above ~ 240 K, the abundance of O decreases dramatically and reactions with O become unimportant. Conversely, the abundance of H₂O increases as neutral-neutral reactions leading to water become important. Using the unmodified Nahoon/KIDA yields a total summation shown by the black dashed line, which is up to $\sim 8\%$ larger than the modified value.

These findings indicate that constraints to the value ζL depend, in part, on using a complete chemical model, knowing the age and temperature of the observed cloud, and using accurate reaction rate coefficients. The calculated abundances n_i also depend on the adopted values for ζ and n_{H_2} in the astrochemical model, implying that one will have to iterate the model in order to achieve convergence with the observations for the quantity ζL . Our experimentally derived thermal rate coefficient reported here helps to improve the reliability of this approach to determining ζL , but it is clear that there are many additional

parameters which also need to be well constrained.

6. Summary

Using a novel merged fast-beams apparatus, we have measured the cross sections for $\text{O} + \text{H}_3^+$ forming OH^+ and H_2O^+ . Our measurements were performed for statistically populated $\text{O}(^3P_J)$ in the ground term and internally hot H_3^+ ($\sim 2500 - 3000$ K). Using state-of-the-art theory as a guide to account for the temperature dependence of the O fine-structure J -levels, we have converted our results into a thermal rate coefficient for forming either OH^+ or H_2O^+ . The good agreement that we find with the two published flowing afterglow measurements at a temperature of ≈ 300 K (and a corresponding level of H_3^+ internal excitation) strongly suggests that the H_3^+ internal excitation does not significantly affect the thermal rate coefficient for this reaction. The Langevin value is in good agreement with our results at 10 K but a factor of 2 higher at 300 K. The two published semiclassical results lie a factor of ~ 1.5 above our results over this temperature range. We have implemented our results into the astrochemical code Nahoon to explore some of the astrophysical implications of our results. For example, for dense clouds at 10 K, we find a reduction in the predicted water abundance by up to nearly 40% at certain times in the lifetime of the cloud.

The authors thank V. Wakelam for stimulating conversations. This work was supported in part by the Advanced Technologies and Instrumentation Program and the Astronomy and Astrophysics Grants Program in the NSF Division of Astronomical Sciences. X.U. is Senior Research Associate of the FRS-FNRS. S.V. was supported in part by the NSF Research Experience for Undergraduates program.

REFERENCES

- Althorpe, S. C., & Clary, D. C. 2003, *ARPC*, 54, 493
- Anicich, V. G., & Futrell, J. H. 1984, *IJMSI*, 55, 189
- Bettens, R. P. A., & Collins, M. A. 1998, *JChPh*, 108, 2424
- . 2001, *JChPh*, 114, 6490
- Bettens, R. P. A., Trevor, A. H., & Collins, M. A. 1999, *JChPh*, 111, 6322
- Bowman, J. M., Czakó, G., & Fu, B. 2011, *PCCP*, 13, 8094
- Bruhns, H., Kreckel, H., Miller, K. A., Urbain, X., & Savin, D. W. 2010a, *PhRvA*, 82, 042708
- Bruhns, H., Kreckel, H., Miller, K., et al. 2010b, *RScI*, 81, 013112
- Fehsenfeld, F. C. 1976, *ApJ*, 209, 638639
- Gentry, W. R., & Giese, C. F. 1977, *JChPh*, 67, 2355
- Herbst, E., & Klemperer, W. 1973, *ApJ*, 185, 505
- Hollenbach, D., Kaufman, M. J., Neufeld, D., Wolfire, M., & Goicoechea, J. R. 2012, *ApJ*, 754, 105
- Huber, K., & Herzberg, G. 1979, *Molecular Spectra and Molecular Structure*, Vol. IV (Springer US), doi:10.1007/978-1-4757-0961-2
- Klippenstein, S. J., Georgievskii, Y., & McCall, B. J. 2010, *JPhChA*, 114, 278
- Kramida, A., Yu. Ralchenko, Reader, J., & NIST ASD Team. 2014, *NIST Atomic Spectra Database* (ver. 5.2), [Online]. Available: <http://physics.nist.gov/asd> [2015, April 9]. National Institute of Standards and Technology, Gaithersburg, MD.

- Kylänpää, I., & Rantala, T. T. 2011, *JChPh*, 135, 104310
- Lee, L. C., & Smith, G. P. 1979, *JChPh*, 70, 1727
- Liu, J., Salumbides, E. J., Hollenstein, U., et al. 2009, *JChPh*, 130, 174306
- McCall, B. J., Geballe, T. R., Hinkle, K. H., & Oka, T. 1999, *ApJ*, 522, 338
- Milligan, D. B., & McEwan, M. J. 2000, *CPL*, 319, 482
- Novotný, O., Buhr, H., Stützel, J., et al. 2010, *JPhChA*, 114, 48704874
- Novotný, O., Becker, A., Buhr, H., et al. 2013, *ApJ*, 777, 54
- O’Connor, A. P., Urbain, X., Stützel, J., et al. 2015, *ApJS*, 219
- Oka, T. 2013, *ChRv*, 113, 8738
- Rienstra-Kiracofe, J. C., Tschumper, G. S., Schaefer, H. F., Nandi, S., & Ellison, G. B. 2002, *ChRv*, 102, 231
- Röhse, R., Kutzelnigg, W., Jaquet, R., & Klopfer, W. 1994, *JChPh*, 101, 2231
- Savić, I., Cermák, I., & Gerlich, D. 2005, *IJMSP*, 240, 139
- Scheer, M., Bilodeau, R. C., Brodie, C. A., & Haugen, H. K. 1998, *PhRvA*, 58, 2844
- Smith, D., & Spanel, P. 1995, *Mass Spectrom. Rev.*, 14, 255
- Wakelam, V., Herbst, E., Loison, J.-C., et al. 2012, *ApJS*, 199, 21
- Wakelam, V., Loison, J.-C., Herbst, E., et al. 2015, *ApJS*, 217, 20

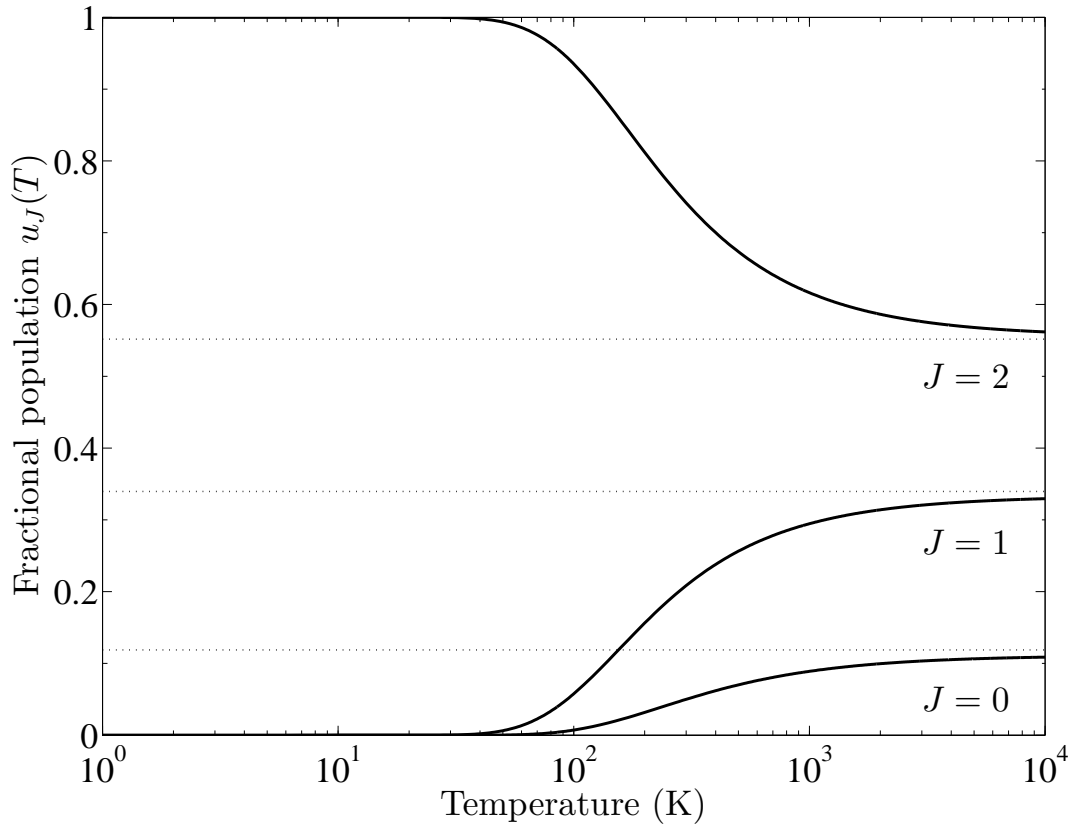


Fig. 1.— $O(^3P_J)$ levels fractional population for a thermal distribution (solid curves) and a statistical distribution (dotted lines).

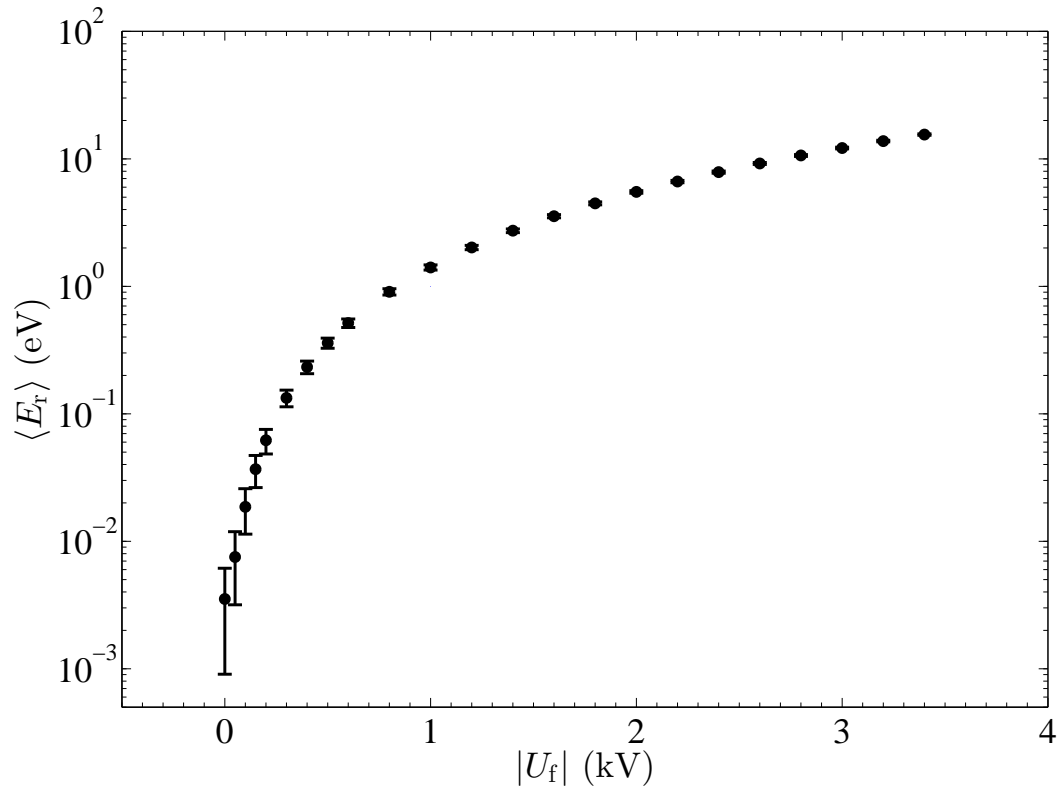


Fig. 2.— Simulated average relative energy $\langle E_r \rangle$ as a function of the floating cell voltage $|U_f|$. The vertical error bars show the full width at half maximum spread of the calculated energy distribution.

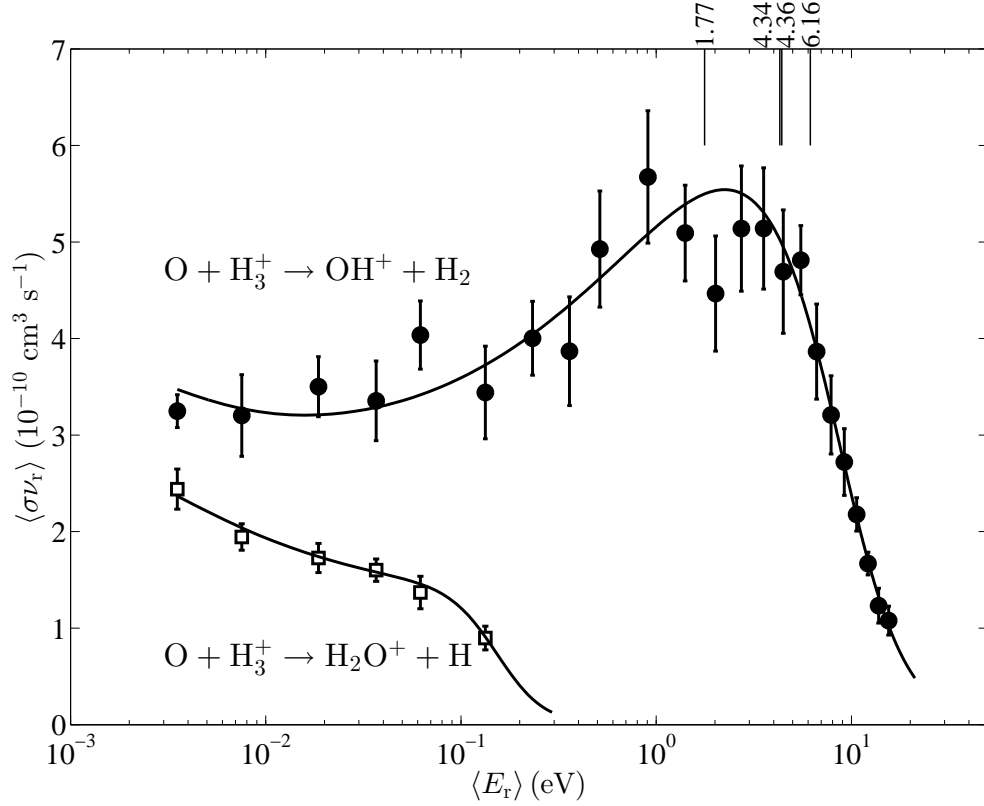


Fig. 3.— Experimental rate coefficients $\langle\sigma v_r\rangle$ as a function of the average relative energy $\langle E_r\rangle$ are shown for Reaction (1) by the filled circles and for Reaction (2) by the open squares. The error bars signify the 1σ statistical uncertainties. Empirical fits to the experimental data using Equation (12) are shown by the solid lines. The vertical lines at the top of the graph show the threshold energies for the competing Reactions (16)-(19) of 1.77, 4.34, 4.36 and 6.16 eV, respectively.

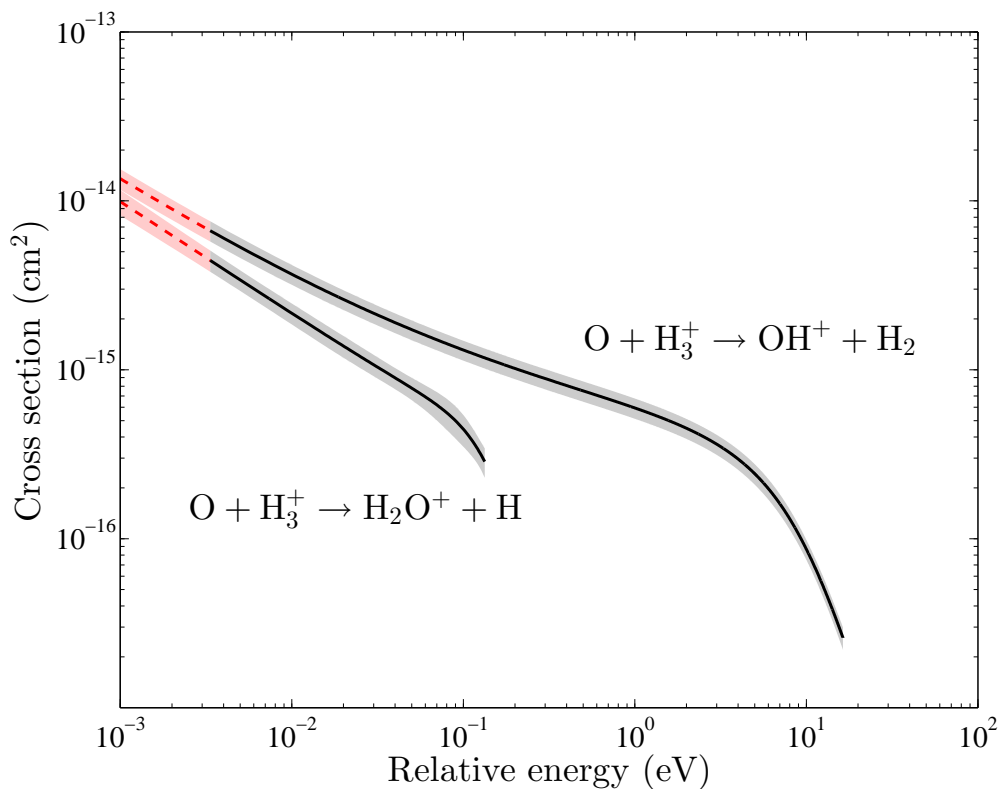


Fig. 4.— The solid black lines show the experimentally derived cross section σ as a function of the average relative energy $\langle E_r \rangle$ for Reactions (1) and (2). The quadrature sum of the 13% systematic uncertainty and the fitting accuracy is denoted by the shaded region. The extrapolation of the experimental results to lower kinetic energies is shown by the red dashed lines and the systematic uncertainty, shown by the surrounding shaded region, is taken as constant using that of the lowest measured energy.

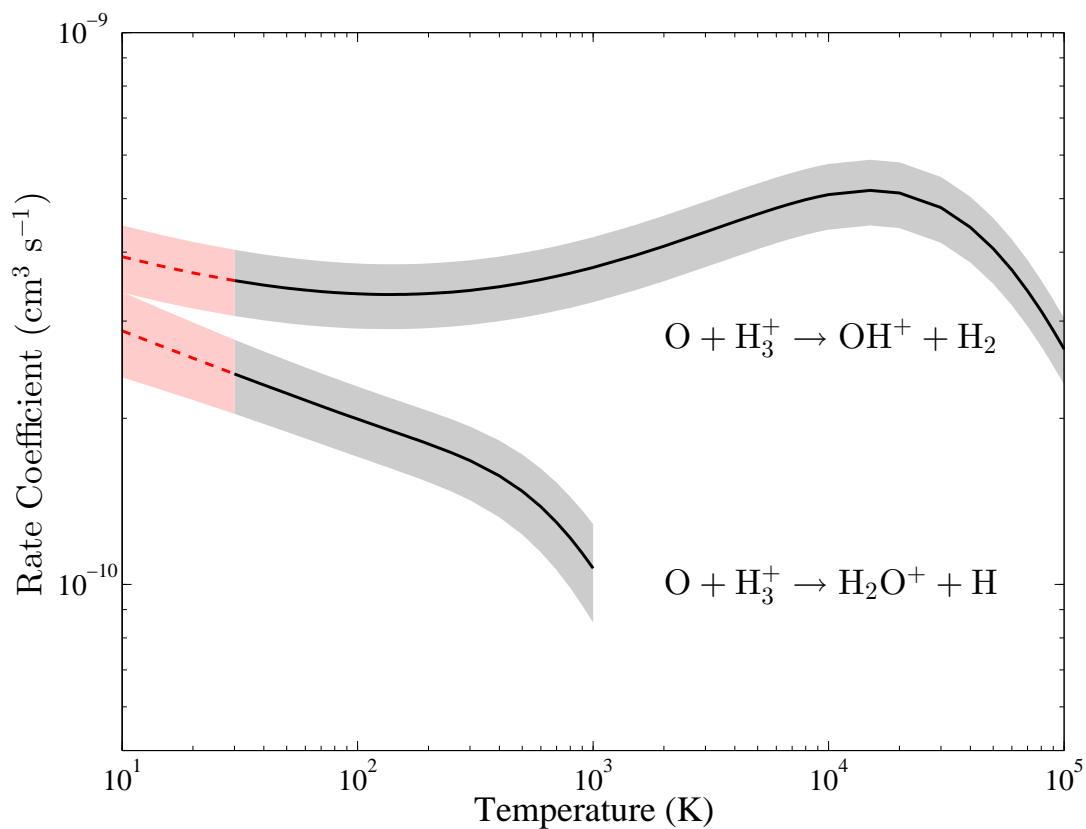


Fig. 5.— Experimentally derived translational temperature rate coefficients vs. temperature for Reactions (1) and (2) are shown by the black solid lines. The quadrature sum of the systematic uncertainty and the fitting accuracy is denoted by the shaded region. The red dashed lines are extrapolations to lower temperatures with the systematic uncertainty (shaded region) taken as constant using that of the lowest measured energy.

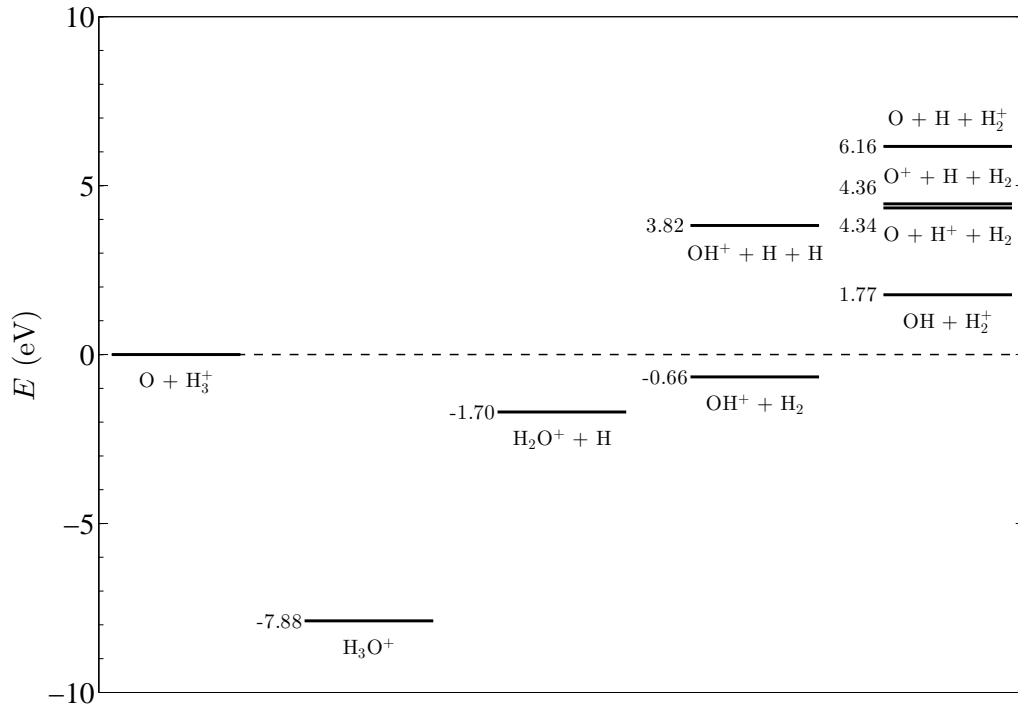


Fig. 6.— Energy level diagram for various $O + H_3^+$ reaction pathways, given in eV, for the various systems in their ground state. Values for H_3O^+ , $H_2O^+ + H$ and $OH^+ + H_2$ are given by Milligan & McEwan (2000); the others are derived from Huber & Herzberg (1979), Röhse et al. (1994), Liu et al. (2009) and Kramida et al. (2014).

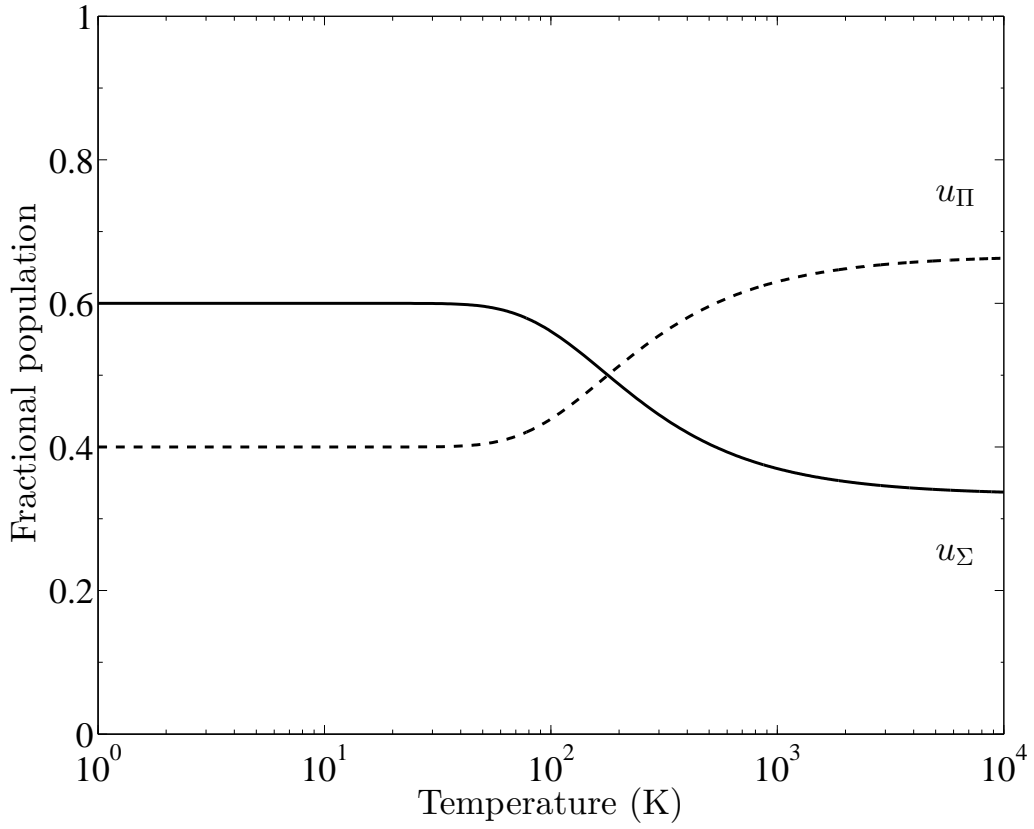


Fig. 7.— Fractional population of the H_3O^+ attractive ${}^3\Sigma$ and repulsive ${}^3\Pi$ symmetries vs. temperature.

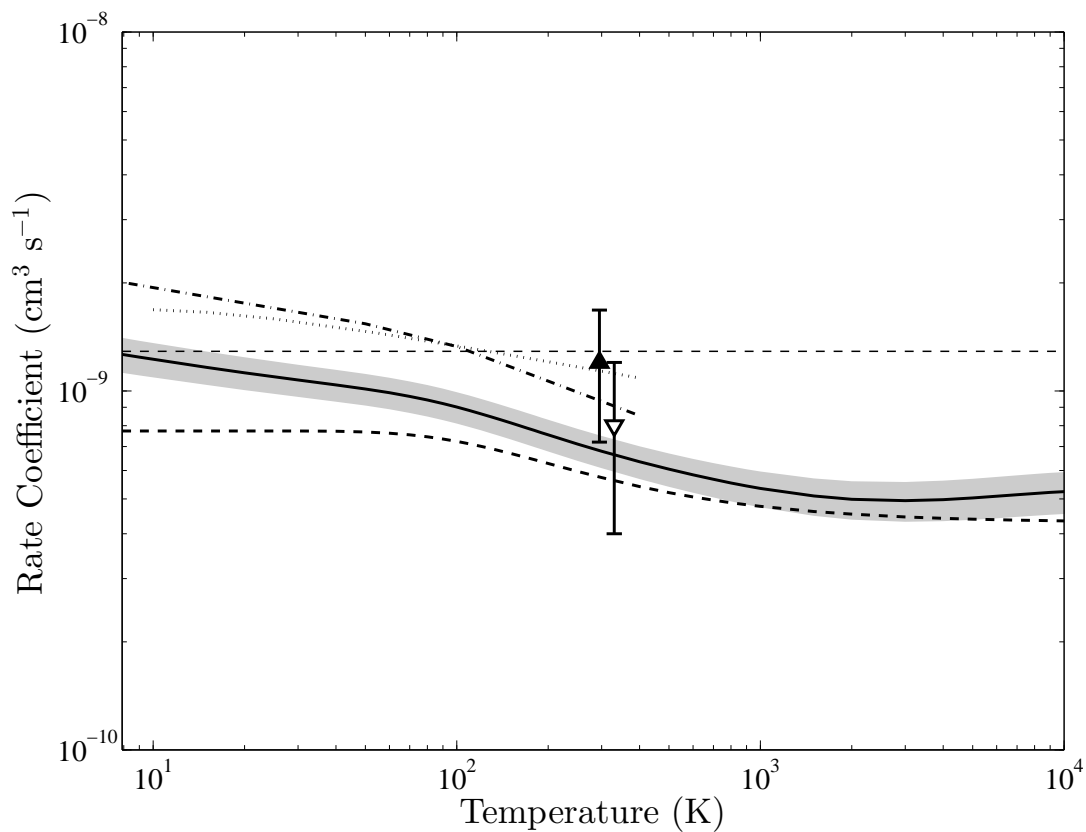


Fig. 8.— Our experimentally derived thermal rate coefficient vs. temperature for the sum of Reactions (1) and (2) is shown by the black solid line. The dashed lines are the Langevin rate coefficient unmodified (thin) and modified (thick). The dotted-dashed lines present the total theoretical calculations of Bettens et al. (1999). The Klippenstein et al. (2010) calculations are shown by the dotted line. The inverted open triangle is the 300 K experimental result of Fehsenfeld (1976) shifted to 330 K for clarity, and the filled triangle the total 295 K experimental result of Milligan & McEwan (2000).

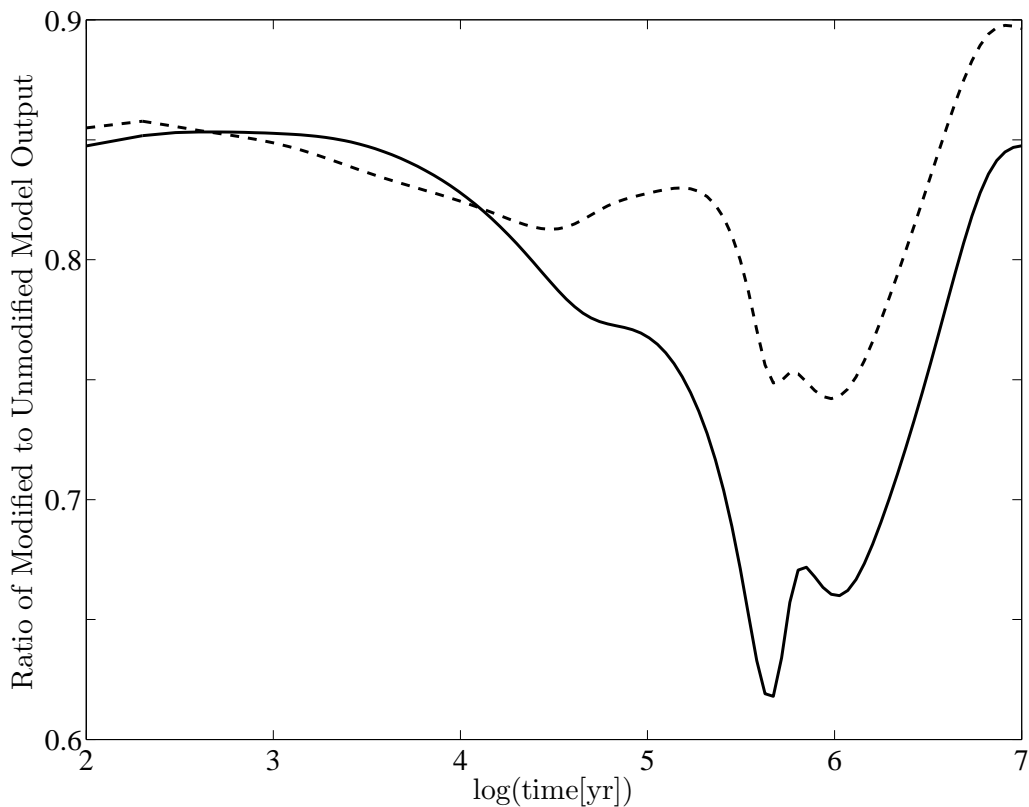


Fig. 9.— Ratio of the modified to unmodified predicted abundances for H_3O^+ (dashed line) and H_2O (solid line). The ratio gives the modified Nahoon/KIDA results using our experimentally derived total rate coefficient for the $\text{O} + \text{H}_3^+$ reaction divided by the unmodified Nahoon/KIDA results, which uses the rate coefficient from Klippenstein et al. (2010).

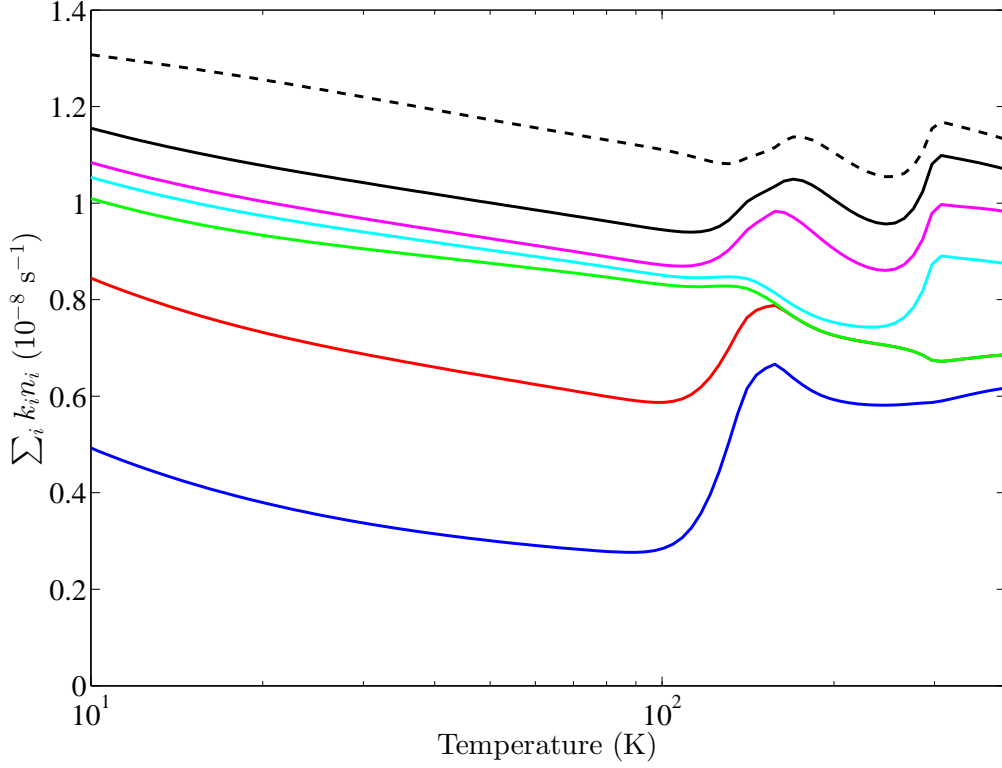


Fig. 10.— Predicted factor $\sum_i k_i n_i$ at a cloud age of 10^5 years using the modified and unmodified Nahoon/KIDA. The solid colored lines correspond to the number of terms being included in the summation for the modified factor, starting with dark blue for just CO, red for the addition of O, green for C, light blue for H_2O , violet for HCN/HNC, and black for the addition of all other species. The predicted factor for all reactants using the unmodified Nahoon/KIDA is shown by the black dashed curve.

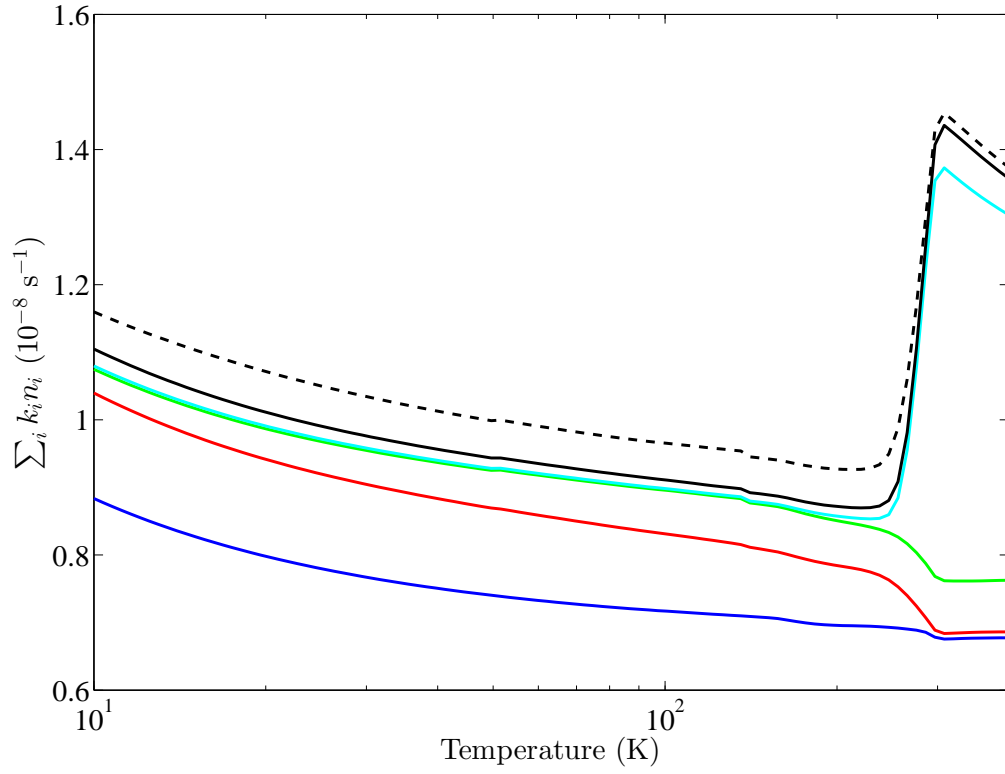


Fig. 11.— Same as Fig. 10 but for a cloud age of 10^6 years. Here the cumulative additions of the reactants $i = \{\text{CO, O, N}_2, \text{H}_2\text{O, all other species}\}$ are shown by the dark blue, red, green, light blue, and black solid lines, respectively.

Table 1: Typical values of the statistical-like uncertainties for Equation (11) for a single data run.

Source	Symbol	Value	Uncertainty (%)
Signal rate	S	1-15 Hz	≤ 4
O velocity	v_n	$5.8 \times 10^7 \text{ cm s}^{-1}$	$\ll 1$
H ₃ ⁺ velocity	v_i	$5.8 \times 10^7 \text{ cm s}^{-1}$	$\ll 1$
O current	I_n	23 nA	5
H ₃ ⁺ current	I_i	225 nA	5
Overlap factor	$\langle \Omega(z) \rangle$	2.7 cm^{-2}	10
Statistical-like uncertainty (single run)			13

Note. - The confidence level for each value is taken as equivalent to a 1σ confidence level. The total statistical-like uncertainty is calculated by treating each individual uncertainty as a random sign error and adding all in quadrature.

Table 2: Same as Table 1 but for the systematic uncertainties for all data runs.

Source	Symbol	Value	Uncertainty (%)
Analyzer transmission	T_a	0.74	3
Grid transmission	T_g	0.90	1
Neutral transmission	T_n	0.94	2
Neutral detector calibration	γ	2.6	12
CEM efficiency	η	0.99	3
Interaction length	L	121.5 cm	2
Total systematic uncertainty			13

Table 3: Fit parameters for the cross section of Reactions (1) and (2) in units of cm^2 for E in eV, using Equation (12).

Reaction	Parameters				
	a_0	$a_{1/2}$	b_1	b_2	b_4
(1)	3.7314E-16	2.1237E-16	-	3.6414E-02	5.0532E-04
(2)	9.8531E-17	-	-4.0668E-02	-4.1891	517.80

Table 4: Fit parameters for the kinetic temperature rate coefficient for Reactions (1) and (2) in units of $\text{cm}^3 \text{s}^{-1}$ for T in K, using Equation (13).

Reaction	Parameters					
	a_0	$a_{1/2}$	a_1	$b_{1/2}$	b_1	$b_{3/2}$
(1)	5.1142E-10	2.6568E-11	9.8503E-15	1.6747E-02	-9.9613E-5	1.1006E-6
(2)	4.2253E-10	-	-	3.4977E-03	-1.4126E-04	6.3584E-05

Table 5. Fit parameters using Equation (22) for the thermal rate coefficient of $\text{O} + \text{H}_3^+$ forming either OH^+ or H_2O^+ .

Parameter	Value		Units
	x	y	
A	7.39	–10	$\text{cm}^3 \text{s}^{-1}$
n	1.46	–1	dimensionless
c_1	6.32	–8	$\text{K}^{3/2} \text{cm}^3 \text{s}^{-1}$
c_2	–3.00	–6	$\text{K}^{3/2} \text{cm}^3 \text{s}^{-1}$
c_3	–1.17	–5	$\text{K}^{3/2} \text{cm}^3 \text{s}^{-1}$
c_4	5.76	–4	$\text{K}^{3/2} \text{cm}^3 \text{s}^{-1}$
T_1	7.47	1	K
T_2	5.40	2	K
T_3	1.83	3	K
T_4	1.90	4	K

Note. — The value for each parameter is given by $x \times 10^y$.